ROYAL SOCIETY OF CHEMISTRY

PAPER

Check for updates

Nanocrystallization of lanthanide-doped KLu$_2$F$_7$–KYb$_2$F$_7$ solid-solutions in aluminosilicate glass for upconverted solid-state-lighting and photothermal anti-counterfeiting†

Shaoxiong Wang,[abc] Jiangkun Chen,[abc] Jidong Lin,[abc] Changbin Yang,[abc] Feng Huang [ID][abc] and Daqin Chen [ID] *[abc]

In situ nanocrystallization of homogeneously distributed Lu–Ln (Lu = La–Lu, Sc) solid-solution potassium lanthanide fluorides inside the same aluminosilicate glass matrix is reported. These precipitated nanocrystals exhibit Ln^{3+} radius dependent phase structures, *i.e.*, cubic K(Lu/Ln)$_3$F$_{10}$ for large-radius Ln^{3+} ions and orthorhombic K(Lu/Ln)$_2$F$_7$ for small-radius Ln^{3+} ones. Particularly, a Lu–Yb system shows the ability to completely substitute between Lu and Yb in the K(Lu/Yb)$_2$F$_7$ nanocrystals, and Er (2 mol%):K(Lu$_{0.5}$Yb$_{0.5}$)$_2$F$_7$@glass yields the best upconversion quantum yield of 0.7%, which is far higher that the value of well-known Yb/Er (20/2 mol%):NaYF$_4$@glass (0.13%). Taking Er/Tm:K(Lu$_{0.5}$Yb$_{0.5}$)$_2$F$_7$@glass as a color converter, a 980 nm laser-driven upconverted lighting device can be constructed to produce bright white-lighting with an optimal luminous efficiency of 0.53 lm W^{-1} and an energy efficiency of 1.31%. In addition, Er:KYb$_2$F$_7$@glass shows a significant photothermal effect owing to 100% Yb^{3+} host ions, leading to 980 nm laser-power-sensitive upconversion luminescence colors. As a proof-of-concept experiment, a specially designed Er:KYb$_2$F$_7$@glass-based flower pattern with tunable upconversion colors is adopted to demonstrate its practical application in high-end anti-counterfeiting.

1. Introduction

Lanthanide (Ln^{3+}) doped upconversion (UC) luminescent materials, which enable the yield of short-wavelength (UV-visible) emissions upon near-infrared (NIR) laser irradiation *via* a multi-photon absorption process, have been widely developed to be applied in optoelectronic fields,[1,2] and impressively, Ln-doped UC nanocrystals (UCNCs) have received extensive attention for their practical applications in bio-imaging, photovoltaics, anti-counterfeiting, therapies and displays.[3–11] In generally, trivalent Yb^{3+} dopants are selected as sensitizers because they have a large absorption cross-section and well match with common 980 nm lasers, and Er^{3+}, Ho^{3+} or Tm^{3+} ions are co-doped into the same host as activators to produce UC emissions through Yb → Ln energy transfer.[12]

For instance, Yb/Er or Yb/Tm doped hexagonal β-NaYF$_4$ NCs have been regarded as one of the most efficient green or blue UC materials.[13–16] Unfortunately, the Yb^{3+} doping content is generally low (∼20%) although highly doping Yb^{3+} can significantly improve the absorption of the incident NIR excitation light.[17] Recently, Er:KYb$_2$F$_7$ UCNCs with 100% Yb^{3+} host ions have been demonstrated to exhibit excellent Er^{3+} ultraviolet UC luminescence properties,[18] but high-content Yb^{3+} dopants can lead to severe concentration quenching and poor UC emissive performance. It is believed that exploring appropriate lanthanide solid-solutions may be a feasible route to achieve high-content Yb doping and efficient UC luminescence, which is worthy of investigation in depth.

On the other hand, there is growing necessity to integrate UC nano-/micro-crystals with a bulk photonic platform to manipulate their excellent optical performance. Traditionally, dispersing UCNCs in polymers was widely adopted to fabricate bulk materials.[19] However, these UCNCs are inclined to agglomerate and their stability is a tough issue. In particular, the products will suffer from damage and invalidation upon high-power NIR laser irradiation, which limits their applications. As an alternative, embedding UCNCs inside inorganic oxide glass (denoted as NCs@glass) is an ideal strategy to address these problems for the facile synthesis, high stability,

[a] College of Physics and Energy, Fujian Normal University, Fujian Provincial Key Laboratory of Quantum Manipulation and New Energy Materials, Fuzhou, 350117, China. E-mail: dqchen@fjnu.edu.cn
[b] Fujian Provincial Collaborative Innovation Center for Optoelectronic Semiconductors and Efficient Devices, Xiamen, 361005, China
[c] Fujian Provincial Engineering Technology Research Center of Solar Energy Conversion and Energy Storage, Fuzhou, 350117, China

This journal is © The Royal Society of Chemistry 2019

J. Mater. Chem. C, 2019, **7**, 14571–14580 | **14571**

high transparency and fearlessness of high-power laser irradiation.[20–22] The NC incorporated glasses can be highly transparent, which will offer a new way to investigate light–NCs interactions in nanocomposites.

Currently, *in situ* glass crystallization is an effective method to produce UCNCs inside glass, and involves the nucleation/growth of NCs *via* ionic diffusion in a glass network and the spatial separation of Ln^{3+} dopants from the glass matrix into the NC lattice.[23–30] However, high requirements are put forward for the precipitated NCs in glass to produce solid-solutions with high-content Yb^{3+} dopants. For example, the host cation must be trivalent and it is necessary for its ionic radius to be close to that of Yb^{3+}. In the family of Ln^{3+} (La^{3+} to Lu^{3+}) including Y^{3+} and Sc^{3+}, Lu^{3+} is the best choice because of the best match of its ionic radius with that of Yb^{3+} sensitizers. In the present work, we investigate the crystallization behaviors of Lu^{3+}-based fluoride solid-solutions in aluminosilicate glasses, and focus on the growth of Lu–Yb solid-solution NCs to achieve highly efficient UC luminescence. A whole-family of Lu–Ln solid-solution fluorides can be precipitated from the same glass matrix, but the crystallized phase structure is highly related to lanthanide radii. A highest UC quantum yield (UCQY) of 0.7% is achieved for Yb/Er (50/2 mol%):KLu_2F_7 NCs@glass, which is much better than that of the well-known Yb/Er (20/2 mol%):β-$NaYF_4$ NCs@glass (0.13%). Benefited from their superior UC performance and remarkable photothermal effect, the as-prepared Lu–Yb NC embedded glasses can find practical applications in NIR-laser-driven UC lighting and high-end anti-counterfeiting. To the best of our knowledge, this is the first report on the fabrication of Lu–Ln solid-solution fluoride NC containing glasses *via in situ* glass crystallization and the related UC optical properties have not been reported to date.

2. Experimental section

Lu–Yb fluoride solid-solution NCs inside glasses were prepared by high-temperature melt-quenching and subsequent heat-treatment. The mole compositions of a series of precursor glasses (PGs) are $100SiO_2$–$6Al_2O_3$–$9K_2O$–$19KF$–$(24 - x)LuF_3$–$xYbF_3$ ($x = 0$–24, mol%). About 15 g of high-purity raw materials with the designed mole ratios were mixed and ground evenly, and then placed in an alumina crucible at 1500 °C for 30 minutes in an ambient atmosphere. The melt was poured into a pre-heated brass mold at 350 °C and then cooled to room temperature to obtain PG. Finally, the NCs@glass products were achieved by heating the corresponding PGs at 600–750 °C for 2 h to induce the crystallization of Lu–Yb fluoride solid-solutions. Other Lu–Ln NCs@glass samples can be prepared by a similar method except for the substitution of YbF_3 by LnF_3 (Ln = La–Lu, Sc) in glass compositions.

To identify the precipitated phases, X-ray diffraction (XRD) patterns were recorded using a powder diffractometer (Mini-Flex600 RIGAKU) with Cu Kα radiation ($\lambda = 0.154$ nm) operating at 40 kV in the 2θ range from 10° to 50°. Microstructure observations of NCs inside glasses were performed on a JEOL JEM-2010 transmission electron microscope (TEM) operated at

200 kV accelerating voltage. Scanning TEM (STEM) images were taken on an FEI aberration-corrected Titan Cubed S-Twin transmission electron microscope operated in a high-angle annular dark-field (HAADF) mode. Photoluminescence (PL), PL excitation (PLE), UC emission spectra, fluorescence decay curves and UCQYs were recorded on an Edinburgh Instruments FLS1000 spectrofluorometer equipped with xenon lamps, pulse xenon lamps, and a 980 nm diode laser as the excitation sources and solid/liquid integrating sphere. UC decay lifetimes were evaluated using the expression $\tau = \int I(t)\mathrm{d}t/I_0$, where I_0 is the peak intensity and $I(t)$ is the time-related emissive intensity. UCQYs were determined *via* the equation $\eta = \dfrac{N_{em}}{N_{abs}} = \dfrac{I_{em}}{I_{blank} - I_{sample}}$, where N_{abs} and N_{em} are the photons absorbed and emitted, respectively; I_{em} is the integrated UC emissive intensity, I_{blank} and I_{sample} are the intensities of the excitation light in the presence of the reference and the product, respectively. The laser power density was measured using an IR Power Meter laser power meter (CNI TS15). The temperature was recorded using a laser sight infrared thermometer (Optris LS) with a temperature resolution of 0.1 °C in the temperature range of −35–900 °C. The temperature data were directly detected from the surfaces of NCs@glass samples. The emissivity coefficient was set to be 0.95. An infrared thermal imager (Fluke Ti10) was employed to characterize the temperature and thermal distribution of the glass samples. The optoelectronic parameters for the GC-based UC white light including luminous flux, radiant flux, luminous efficiency (LE), energy efficiency and Commission Internationale de L'Eclairage (CIE) color coordinates were measured by using a sphere spectroradiometer system consisting of a high-power 980 laser source (MDL-III980-3W, CNI, China) and an integrating sphere (Labsphere Inc., USA).

3. Results and discussion

As tabulated in Table S1 (ESI†), a series of glass compositions of $100SiO_2$–$6Al_2O_3$–$9K_2O$–$19KF$–$16LuF_3$–$9LnF_3$ (Ln = La–Lu, and Sc) with a Lu-to-Ln ratio of 16 : 9 were designed. The NCs@glass samples were fabricated by heating PGs at 750 °C for 2 h and the corresponding XRD patterns are shown in Fig. 1a. Interestingly, as the Ln^{3+} ionic radius decreases from La to Sc (Table S2, ESI†), the crystallized NCs inside glass show a gradual change from the cubic $K(Lu/Ln)_3F_{10}$ phase to the orthorhombic $K(Lu/Ln)_2F_7$ phase (Table S1, ESI†). Similar results can be found in the PGs (Fig. S1, ESI†), indicating that self-crystallization has already occurred in these glasses. Notably, the diffraction peaks gradually shift toward higher angle with alteration of Ln^{3+} dopants from La to Sc. This is believed to be attributed to the formation of Lu–Ln fluoride solid-solutions, where a lanthanide contraction effect will result in lattice contraction. To confirm this, verification experiments were performed *via* the complete substitution of Lu^{3+} by Ln^{3+} in glass (Fig. S2, ESI†). XRD patterns evidence that the corresponding diffraction peaks move toward smaller angle after replacing Lu^{3+} and some minor impurity phases appear (Fig. S2, ESI†). These results verify that the crystallized phases in glasses are indeed Lu–Ln fluoride solid-solutions and
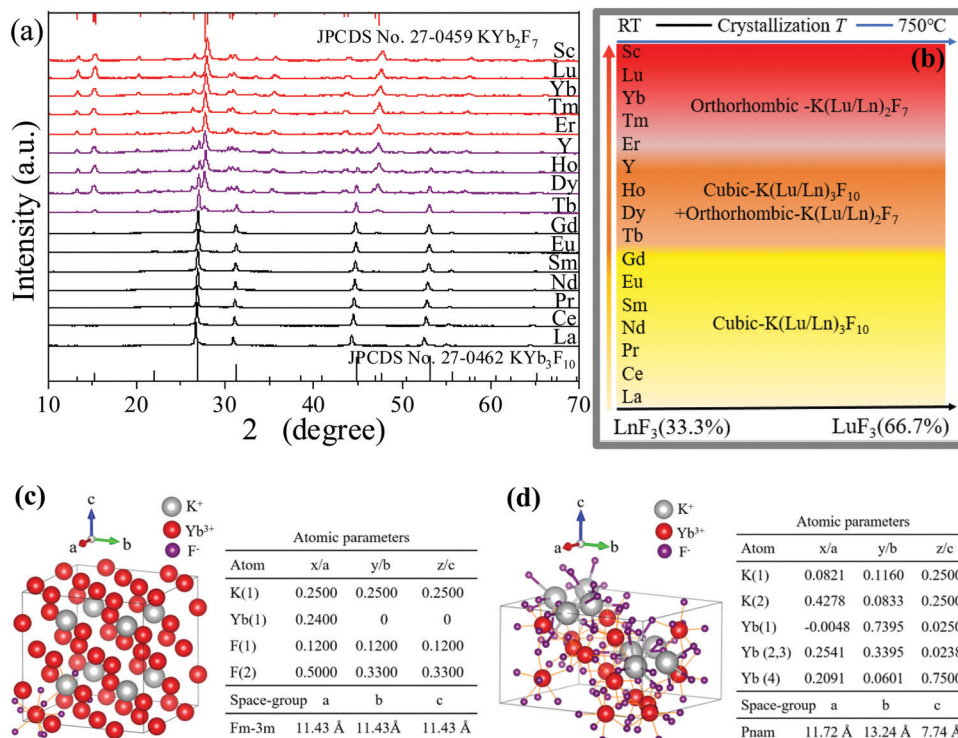
14572 | *J. Mater. Chem. C*, 2019, **7**, 14571–14580

This journal is © The Royal Society of Chemistry 2019

Fig. 1 (a) XRD patterns of Lu–Ln solid-solution NCs@glass prepared by heating PGs at 750 °C for 2 h. The diffraction bars represent cubic KY_3F_{10} (JPCDS No. 27-0462) and orthorhombic KYb_2F_7 (JPCDS No. 27-0459) crystals. (b) The variation of the crystallized phase structures inside glass with change of Ln dopants. (c and d) Schematic illustrations of crystal structures and crystallographic data of cubic KYb_3F_{10} and orthorhombic KYb_2F_7.

Lu^{3+} ions are beneficial to the formation of pure $K(Lu/Ln)_3F_{10}$ or $K(Lu/Ln)_2F_7$ solid-solutions. As evidenced in Fig. S3 (ESI†), different crystallization temperatures (600–750 °C) have no influence on the precipitated crystalline phase. Accordingly, a schematic phase diagram is plotted in Fig. 1b, which illustrates that the variation of the precipitated Lu–Ln solid-solution crystal structures from cubic $K(Lu/Ln)_3F_{10}$ (Fig. 1c) to orthorhombic $K(Lu/Ln)_2F_7$ (Fig. 1d) is closely connected with Ln^{3+} ionic radius contraction. Interestingly, Lu–Ln solid-solutions with relatively large Ln^{3+} ions (Ln = La, Ce, Pr, Nd, Sm, Eu, Gd and Tb) tend to be in the cubic phase. When the Ln^{3+} ionic radius further contracts to a certain extent, the orthorhombic $K(Lu/Ln)_2F_7$ (Ln = Er, Tm, Yb, Lu, Sc) solid-solutions are formed inside the glass matrix. This phenomenon may be attributed to the influence of both glass-network-limited nucleation/growth and the lanthanide contraction effect, which needs further investigation.

TEM observations on Lu–Gd, Lu–Yb and Lu–Sc NCs@glass samples indeed confirm the precipitated $K(Lu/Gd)_3F_{10}$, $K(Lu/Yb)_2F_7$ and $K(Lu/Sc)_2F_7$ nanoparticles from the glass matrix (Fig. 2a–c). The presence of NCs with bright contrast inside the aluminosilicate glass matrix can be clearly identified in HAADF-STEM images and the particle sizes are in the range of 50–80 nm (Fig. 2d–f). The corresponding element mappings confirm the segregation of Lu and Gd/Yb/Sc in the NCs and the homogeneous distribution of K and F in the particles and the glass matrix. These results prove the successful formation of $K(Lu/Gd)_3F_{10}$, $K(Lu/Yb)_2F_7$ and $K(Lu/Sc)_2F_7$ solid-solution NCs in glass after crystallization treatment.

To further identify the location of activators in NCs@glass, Eu^{3+} dopants were used as structural probes. As evidenced in Fig. S4a and b (ESI†), Eu^{3+} doping did not modify the crystallization behaviors of the samples, and the precipitated crystal phases inside glass were not affected. The related PL spectra of Eu^{3+} single-doped PG and NCs@glass were recorded, as presented in Fig. 3a and b. Characteristic Eu^{3+} emissions from $^5D_J \rightarrow {}^7F_J$ (J = 0, 1, 2, 3) were observed for all the samples. Obviously, the emission bands of NCs@glass samples show more distinct Stark-splitting, and the decay lifetime is elongated compared with that of the PG sample (Figure S4c–h, ESI†). Additionally, the intensity ratio between electric-dipole $^5D_0 \rightarrow {}^7F_2$ transition and $^5D_0 \rightarrow {}^7F_1$ magnetic dipole one significantly decreases, indicating that heat-treatment plays an important role in promoting partition of Eu^{3+} ions into $K(Lu/Ln)_3F_{10}$ and $K(Lu/Ln)_2F_7$ crystalline lattices.

In a further experiment, Yb^{3+} and Er^{3+} dopants with doping contents of 20 mol% and 2 mol% were introduced into glasses. It is noted that only La–Lu, Gd–Lu, Y–Lu, Yb–Lu, Lu–Lu and Lu–Sc samples can produce bright UC luminescence. The corresponding UC emission spectra of PGs and NCs@PG sample obtained by heat-treatment at various temperatures (600, 650, 700, and 750 °C) for 2 h are provided in Fig. 3c and Fig. S5 (ESI†). All the products exhibited typical $^2H_{11/2}, {}^4S_{3/2} \rightarrow {}^4I_{15/2}$ (green) and $^4F_{9/2} \rightarrow {}^4I_{15/2}$ (red) transitions of Er^{3+} under 980 nm laser excitation. With an increase of crystallization temperature, UC emissive intensity gradually enhances (Fig. 3d), while the red-to-green UC intensity ratio monotonously decreases (Fig. 3c). It is a typical feature that more and more Yb/Er dopants separate into
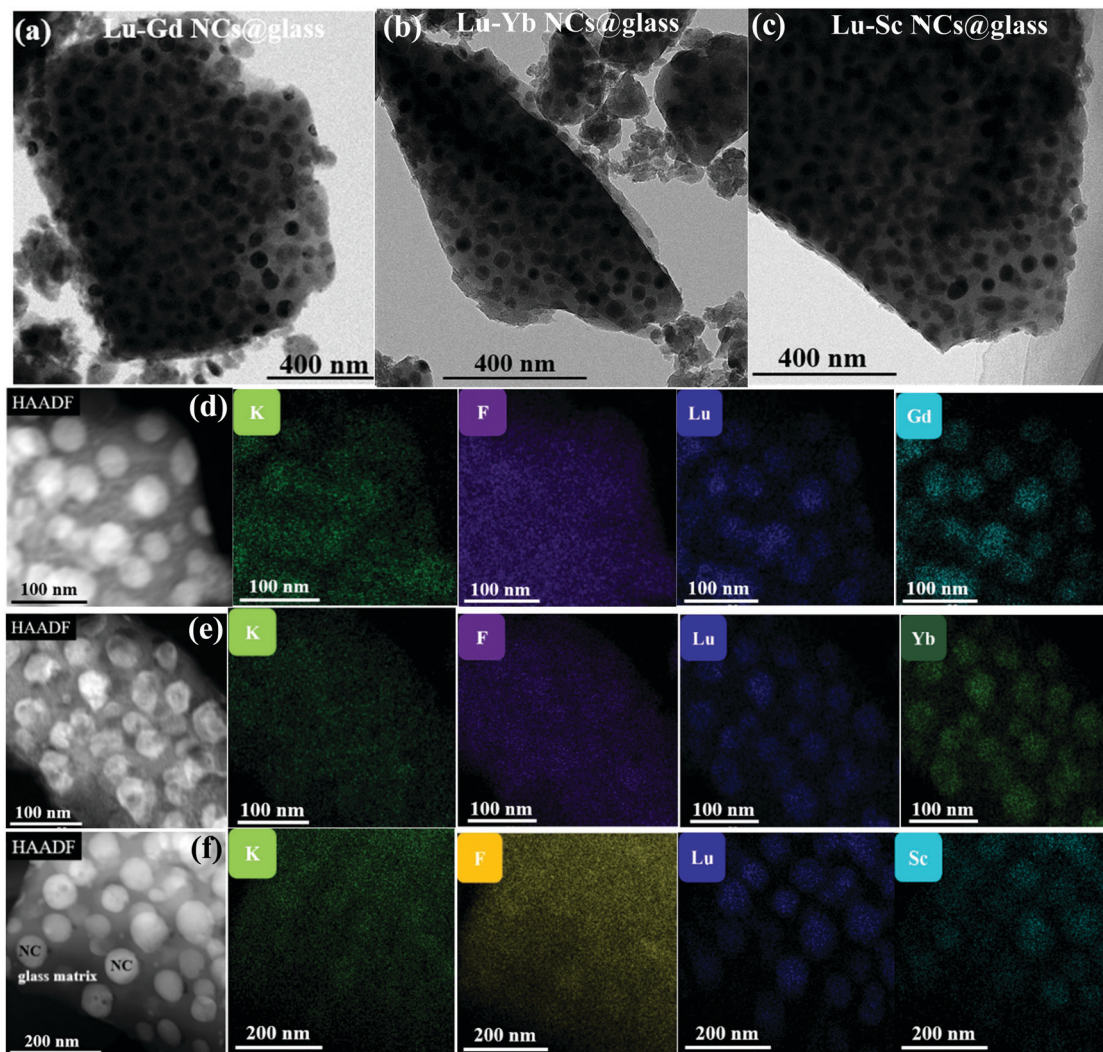
Fig. 2 TEM and HAADF–STEM images of (a and d) K(Lu/Gd)$_3$F$_{10}$, (b and e) K(Lu/Yb)$_2$F$_7$ and (c and f) K(Lu/Sc)$_2$F$_7$ NCs@glass samples associated with K, F, Lu, Gd, Yb and Sc element mappings.

Lu–Ln solid-solution crystal lattices with improved crystallinity. For UC materials, longer fluorescence lifetime usually means higher emissive efficiency.[31] Taking Lu–Sc NCs@glass as a typical example, UC decay curves by monitoring Er^{3+} ^{4}S$_{3/2}$ and ^{4}F$_{9/2}$ emissions were recorded under 980 nm pulse laser excitation, as exhibited in Fig. 3e and f. Apparently, with the increase of crystallization temperature, the evaluated UC lifetime gradually increases from ~0.4 ms to ~1.2 ms, being consistent with the variation of emission intensity. Similarly, the extended trend of decay lifetime with an increase of heat-treatment temperature can be observed for all the other Lu–Ln NCs@glass samples (Fig. S6, ESI†). All these results confirmed that the emitting centers can be separated from glass into the precipitated Lu–Ln solid-solution NCs upon increasing the crystallization temperature.

From a previous discussion, it is known that the Yb/Er doped Lu–Ln (Ln = La, Gd, Y, Yb, Lu, Sc) NCs@glass samples after heat-treatment at 750 °C have maximal UC emission intensity, and the corresponding UC spectra are shown in Fig. 4a. All the samples show similar spectral profiles except

the Lu–Yb NCs@glass one. This is attributed to high-content Yb^{3+} ions in the solid-solution NCs, where red UC emission dominates. Impressively, compared with other samples, Lu–Yb NCs@glass exhibits the highest UCQY of Er^{3+} (Fig. 4b), which is probably owing to the high-content Yb^{3+} ions in the Lu–Yb solid-solution host. In the following section, we will conduct in-depth research on the Lu–Yb system.

To examine the effect of Yb^{3+} doping concentration on the structure and UC luminescence, we further designed a series of glass composition with an increase of Yb^{3+} content (0–100%) to replace Lu^{3+} in the K(Lu/Yb)$_2$F$_7$ crystalline lattice (Table S3, ESI†). All the samples were doped with 2 mol% Er^{3+} emitting centers. As shown in Fig. 5a, the XRD patterns indicate that the orthorhombic Lu–Yb solid-solution NCs can be precipitated from glass even when Lu^{3+} ions are completely substituted Yb^{3+} ones, which may benefit from their approximate ionic radii (r_{Lu} = 1.00 Å and r_{Yb} = 1.01 Å) and electronic configurations. UC spectra exhibit significant variation of green and red emissions (Fig. 5b), and the UC emissive color changes from pure green to
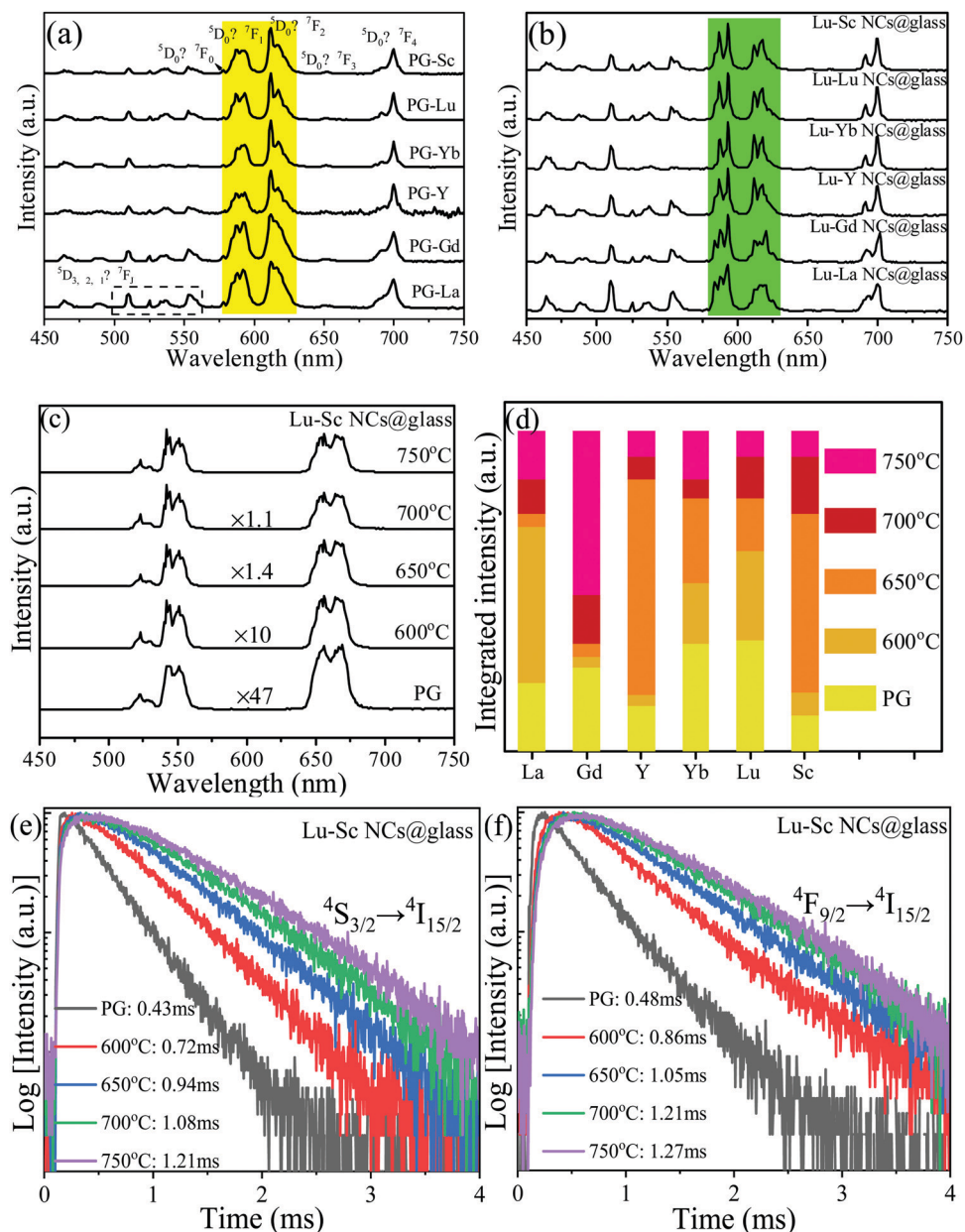
Fig. 3 PL spectra (λ_{ex} = 393 nm) of Eu-doped (a) PG and (b) Lu−Ln NCs@glass prepared by heating PG at 750 °C for 2 h. (c) UC emission spectra (λ_{ex} = 980 nm) of Yb/Er-doped Lu−Sc NCs@glass samples fabricated at different crystallization temperatures. (d) The crystallization temperature dependent UC integrated intensities and decay curves by monitoring (e) 545 nm and (f) 650 nm emissions. The evaluated UC decay lifetimes are provided in (e and f).

pure red with an increase of Yb^{3+} content (inset of Fig. 5b). This is attributed to the enhanced energy transfer from Yb to Er, which induces remarkable population of the Er^{3+} $^4F_{9/2}$ red-emitting state. As demonstrated in Fig. 5c, the red-to-green (R/G) intensity ratio monotonously increases when the Yb^{3+} content increases from 0% to 100%, while the integrated red and green intensities show an optimal Yb^{3+} content in the range of 30–50 mol%. Compared to the well-known hexagonal Yb/Er (20/2 mol%):β-NaYF$_4$ NCs,[13–16] the concentration quenching effect is suppressed to a certain degree for the present Lu–Yb solid-solution NCs. For quantitative comparison, laser power dependent UCQYs for the Yb/Er (50/2 mol%):KLu$_2$F$_7$ NCs@glass

and Yb/Er (20/2 mol%):β-NaYF$_4$ NCs@glass were recorded and are presented in Fig. 5d, respectively. The Yb/Er:β-NaYF$_4$@glass was prepared via elaborate design of glass composition and a similar glass crystallization strategy, and the particle sizes of β-NaYF$_4$ inside glass were tuned to be close to those of Yb/Er:KLu$_2$F$_7$ ones to enable the comparison of UC performance (Fig. S7, ESI†). Evidently, the absolute UCQYs of Yb/Er:KLu$_2$F$_7$ NCs@glass are better than those of Yb/Er:β-NaYF$_4$ NCs@glass upon the excitation of different laser powders. Specifically, the maximal UCQY of Yb/Er:KLu$_2$F$_7$ NCs@glass can reach as high as 0.7%, which is far higher than that of Yb/Er:β-NaYF$_4$ NCs@glass (∼0.13%). These results certainly confirm the excellent UC

This journal is © The Royal Society of Chemistry 2019

J. Mater. Chem. C, 2019, 7, 14571–14580 | 14575

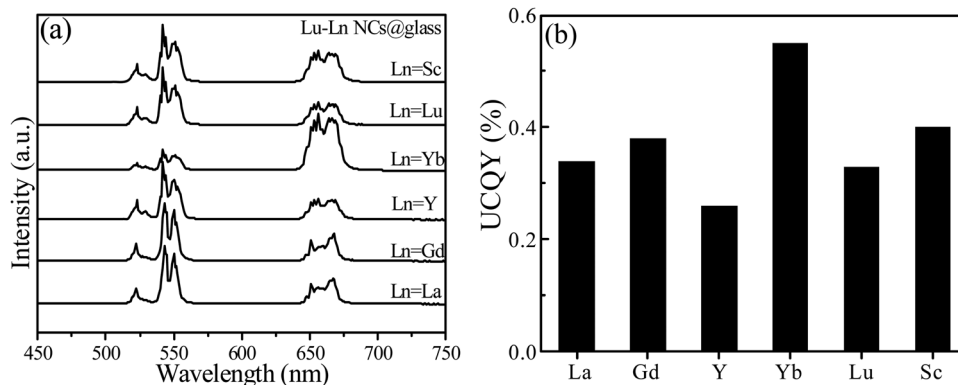**Fig. 4** (a) UC emission spectra (λ_{ex} = 980 nm) of Yb/Er-doped Lu−Ln NCs@glass samples and the corresponding UCQY values recorded with a laser power density of 60 W cm^{-2}.

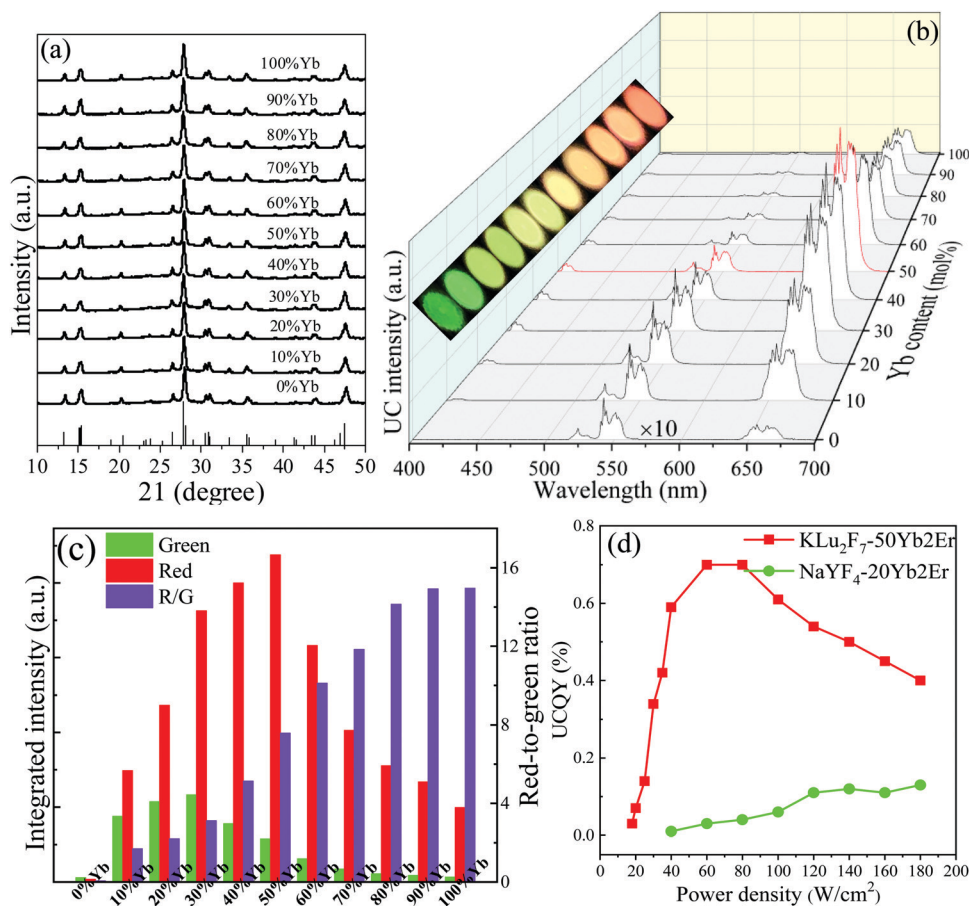**Fig. 5** (a) XRD patterns and (b) UC emission spectra of Lu (1 − x mol%)−Yb (x mol%) NCs@glass samples with gradual substitution of Lu by Yb dopants (x = 0, 10, 20, 30, 40, 50, 60, 70, 80, 90, 100). The diffraction bars represent orthorhombic KYb$_2$F$_7$ (JPCDS No. 27-0459) crystals. Insets of (b) show the corresponding UC luminescence photographs upon 980 nm laser irradiation. (c) Yb-content-dependent green and red UC integrated intensities and red-to-green ratios (R/G). (d) UCQY values of Yb/Er (50/2 mol%) doped KLu$_2$F$_7$ NCs@glass versus laser power density. The values of Yb/Er (20/2 mol%) doped hexagonal NaYF$_4$ NCs@glass are presented in (d) for comparison.

performance for the present high-content Yb^{3+} doped NCs@glass samples.

Benefited from their tunable UC emissions and high UCQYs, the as-prepared Lu–Yb NCs@glass samples can be adopted as color converters in NIR laser-driven UC white light. As shown in

Fig. 6a, Er:K(Lu$_{0.5}$Yb$_{0.5}$)$_2$F$_7$ NCs@glass yields green (Er^{3+}: ^{2}H$_{11/2}$, ^{4}S$_{3/2}$ → ^{4}I$_{15/2}$) and red (Er^{3+}: ^{4}F$_{9/2}$ → ^{4}I$_{15/2}$) emissions, and Tm:K(Lu$_{0.5}$Yb$_{0.5}$)$_2$F$_7$ NCs@glass produces blue (Tm^{3+}: ^{1}D$_2$ → ^{3}F$_4$, ^{1}G$_4$ → ^{3}H$_6$) and red (Tm^{3+}: ^{1}G$_4$ → ^{3}F$_4$) emissions.[12] In this case, red/green/blue (RGB) three primary emissions can be

14576 | J. Mater. Chem. C, 2019, 7, 14571−14580

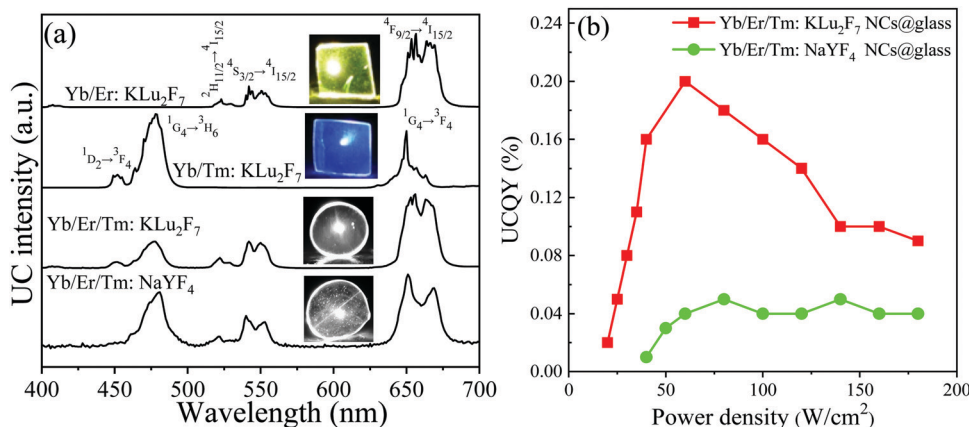This journal is © The Royal Society of Chemistry 2019

Fig. 6 (a) UC emission spectra of Yb/Er, Yb/Tm, and Yb/Er/Tm doped KLu_2F_7 NCs@glass samples and Yb/Er/Tm doped $NaYF_4$ NCs@glass. (b) Comparison of white-light UCQYs for Yb/Er/Tm (50/0.5/0.2 mol%):KLu_2F_7 NCs@glass and Yb/Er/Tm (20/0.45/0.25 mol%):$NaYF_4$ NCs@glass under irradiation of a 980 nm laser with different power densities.

achieved *via* co-doping Er^{3+} and Tm^{3+} activators into $K(Lu_{0.5}Yb_{0.5})_2F_7$ NCs@glass, leading to white light luminescence under the irradiation of a 980 nm laser. The optimal contents for Er^{3+} and Tm^{3+} dopants are 0.5 mol% and 0.2 mol%, respectively. As a comparison, Yb/Er/Tm (20/0.45/0.25, mol%):$NaYF_4$ NCs@glass was prepared, which can also lead to white light UC luminescence (Fig. 6a). Laser-power-dependent UCQYs for the Yb/Er/Tm (50/0.5/0.2 mol%):KLu_2F_7 NCs@glass and Yb/Er/Tm (20/0.45/0.25 mol%): $NaYF_4$ NCs@glass were recorded and are provided in Fig. 6b. Impressively, the UCQY values of Yb/Er/Tm:KLu_2F_7 NCs@glass are better than those of Yb/Er/Tm:$NaYF_4$ NCs@glass for all the different pumping laser power densities, certifying that the Yb/Er/Tm:KLu_2F_7 NCs@glass is a highly efficient UC white-light host material and is expected to be suitable for NIR laser-driven UC solid-state lighting.

The optoelectronic parameters for the constructed NIR laser-driven UC lighting device using NCs@glass samples were systematically evaluated using a sphere–spectroradiometer system with a transmissive configuration (Fig. 7a).[32,33] The devices produce bright white light and the brightness significantly enhances with an increase of incident laser power (Fig. 7b). The corresponding laser power dependent UC emission spectra of Yb/Er/Tm:$NaYF_4$ NCs@glass and Yb/Er/Tm:KLu_2F_7 NCs@glass were recorded and are shown in Fig. 7c and d, respectively. With an increase of laser power, blue, green and red tri-color UC emissions are remarkably enhanced. Tm^{3+} blue UC emissions are three- ($^1G_4$) or four-photon ($^1D_2$) processes while both Er^{3+} green and red emissions are two-photon processes.[12] Therefore, Tm^{3+} UC intensity shows a more significant increase than Er^{3+} ones for the Yb/Er/Tm:$NaYF_4$ NCs@glass sample, which leads to a shift of color coordinates from white light to the blue one. However, for the Yb/Er/Tm:KLu_2F_7 NCs@glass sample, only a slight increase in Tm^{3+} blue luminescence relative to Er^{3+} green and red ones is observed, which is probably owing to the saturated absorption of high-content Yb^{3+} sensitizers and the different effects of laser power on the population of different ion levels. In addition, green UC emission ($\sim$520 nm) attributed to the Er^{3+}: $^2H_{11/2} \rightarrow {}^4I_{15/2}$ transition shows a significant enhancement upon an increase of laser power. This is due to the increased electron

population in the Er^{3+} $^2H_{11/2}$ excited state *via* laser-induced thermal activation from the thermally coupled Er^{3+} $^4S_{3/2}$ state for the high-content Yb^{3+} doped KLu_2F_7 NCs@glass sample. As a consequence, different to the case of Yb/Er/Tm:$NaYF_4$ NCs@glass, the color coordinates of Yb/Er/Tm:KLu_2F_7 NCs@glass can remain in the region of white light with an increase of laser power. The optoelectronic parameters for the NCs@glass-based lighting devices are presented in Fig. 7e–h. Both the luminous flux and the radiant flux of the devices increase with an increase of laser power density (Fig. 7e and g). At high laser power density, the lighting performance of KLu_2F_7 NCs@glass is obviously better than that of $NaYF_4$ NCs@glass, which is consistent with previous results of UCQYs. Specifically, the luminous efficiency of KLu_2F_7 based lighting can reach 0.53 lm W^{-1} with an energy efficiency of 1.31%, while those of $NaYF_4$ based lighting are 0.26 lm W^{-1} and 0.36%, respectively (Fig. 7f and h). Therefore, it can be concluded that the as-prepared $Er/Tm:K(Lu_{0.5}Yb_{0.5})_2F_7$ NCs@glass is a stable and appropriate UC nanocomposite for constructing NIR laser-driven UC solid-state-lighting.

Impressively, it is found that the $Er:Cs(Lu/Yb)_2F_7$ NCs@glass exhibits obvious 980 nm laser-power-sensitive UC luminescence (Fig. S8 ESI,† and Fig. 8a), where 520 nm green emission assigned to the Er^{3+} $^2H_{11/2} \rightarrow {}^4I_{15/2}$ transition relative to 545 nm one attributed to the Er^{3+} $^4S_{3/2} \rightarrow {}^4I_{15/2}$ transition gradually enhances with an increase of laser power. This is attributed to the laser-induced photothermal effect, which leads to significantly increased electron population in the Er^{3+} $^2H_{11/2}$ excited state *via* laser-induced thermal activation from the thermally coupled Er^{3+} $^4S_{3/2}$ state.[34] To quantitatively and visually characterize laser-induced temperature variation in these samples, real-time infrared thermal images with 980 nm laser irradiation on $Er:K(Lu_{0.9}Yb_{0.1})_2F_7$ NCs@glass, $Er:K(Lu_{0.5}Yb_{0.5})_2F_7$ NCs@glass and $Er:KYb_2F_7$ NCs@glass were recorded (Fig. 8b). It is evidenced that the temperature gradually increases with an increase of laser power for all the samples, but the temperature in the 100 mol% Yb sample increases much faster than those in the low-content Yb samples. High-content Yb^{3+} in the sample can effectively absorb
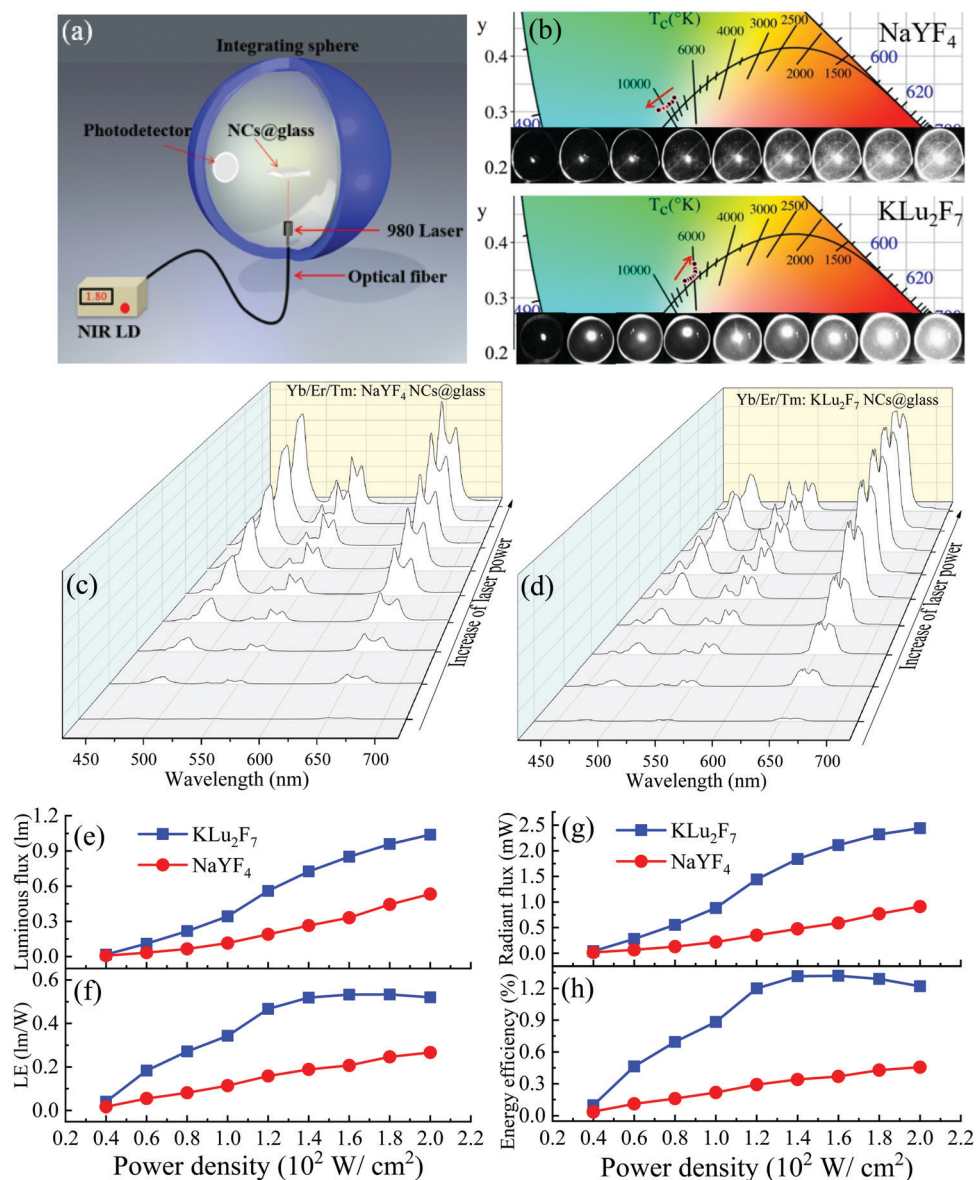
Fig. 7 (a) Schematic illustration of the measurement system for NIR-laser-driven UC lighting. (b) CIE color coordinates *versus* laser power density for the constructed UC lighting devices. Insets show the corresponding UC lighting photographs. Laser power density dependent UC emission spectra for (c) Yb/Er/Tm doped NaYF$_4$ NCs@glass and (d) KLu$_2$F$_7$ NCs@glass, respectively. Optoelectronic parameters of (e) luminous flux, (f) luminous efficiency, (g) radiant flux and (h) energy efficiency *versus* laser power density.

the incident 980 nm laser and a large amount of the absorbed energy can be used to heat the sample. The exact temperature of Er:KYb$_2$F$_7$ NCs@glass detected from a laser sight infrared thermometer is presented in Fig. 8c. The temperature can reach up to 600 °C upon 275 W cm^{-2} laser irradiation. The remarkable laser-induced photothermal effect for the Er:KYb$_2$F$_7$ NCs@glass sample enables it to find novel anti-counterfeiting application. As evidenced in Fig. 8d and Table S4 (ESI†), the UC emissive color gradually changes from red to yellow-green with an increase of laser power and color coordinates in the CIE diagram show a similar variation. As a proof-of-concept experiment, a Chinese Dehua porcelain decorated with Er:KYb$_2$F$_7$ NCs@glass can yield a red UC flower pattern when exposed to a low-power laser (60 mW) and

the UC color of the lower pattern changes to yellow after the laser power increases up to 250 mW (inset of Fig. 8d).

4. Conclusions

In summary, this study offers a facile crystallization route to realize the growth of a whole-family of potassium lanthanide fluoride solid-solution NCs in aluminosilicate glass. The crystallized phase structure is highly related to lanthanide radii, and converts from cubic K(Lu/Ln)$_3$F$_{10}$ to orthorhombic K(Lu/Ln)$_2$F$_7$ accompanied by lanthanide contraction. Importantly, Lu and Yb in K(Lu/Ln)$_2$F$_7$ NCs are completely interchangeable,
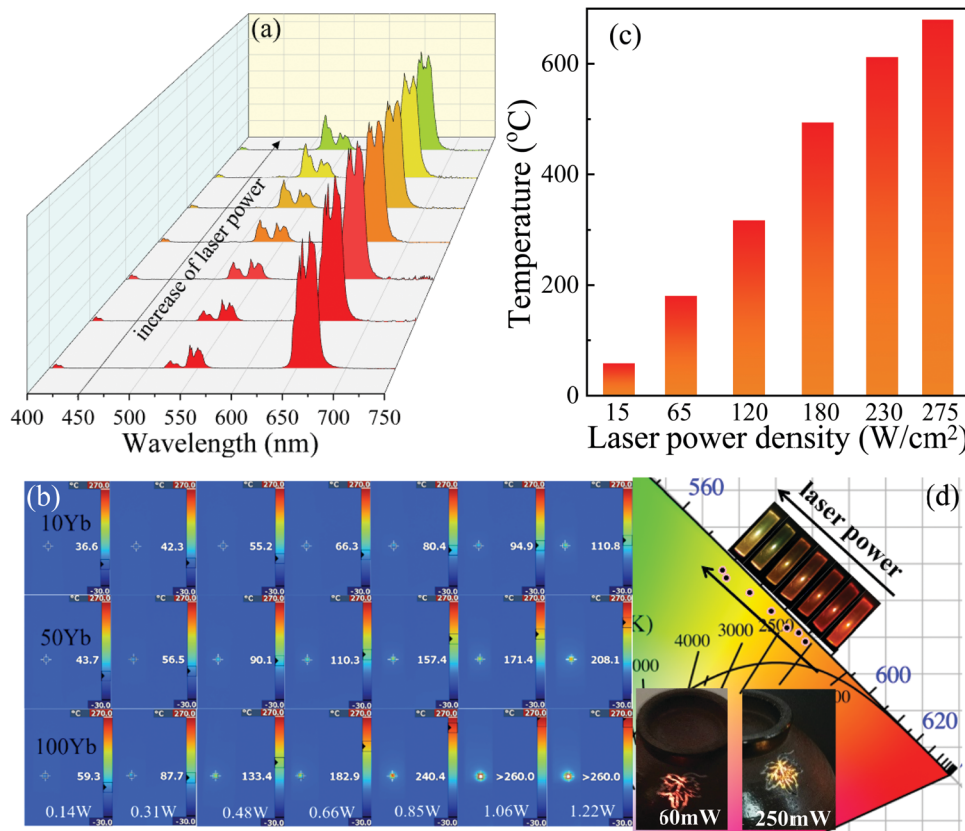
Fig. 8 (a) Laser power dependent UC emission spectra of Er:KYb$_2$F$_7$ NCs@glass (all the spectra are normalized at Er^{3+} 545 nm emission assigned to $^4S_{3/2} \rightarrow {}^4I_{15/2}$ transition). (b) Infrared thermal images recorded from Er:K(Lu$_{0.9}$Yb$_{0.1}$)$_2$F$_7$ NCs@glass (first row), Er:K(Lu$_{0.5}$Yb$_{0.5}$)$_2$F$_7$ NCs@glass (second row) and Er:KYb$_2$F$_7$ NCs@glass (third row) under irradiation of a 980 nm laser (laser power gradually increases from left to right: 0.14, 0.31, 0.48, 0.66, 0.85, 1.06 and 1.22 W). The detected temperatures are provided in each figure. (c) The experimentally measured temperatures for the Er:KYb$_2$F$_7$ NCs@glass exposure to different 980 nm laser power densities. (d) Laser power dependent UC luminescence photographs and CIE color coordinates. The inset shows the anti-counterfeiting demonstration of Chinese Dehua porcelain decorated by an Er:KYb$_2$F$_7$ NCs@glass flower pattern.

and Er^{3+}-doped K(Lu$_{0.5}$Yb$_{0.5}$)$_2$F$_7$ NCs@glass possesses much higher UCQY (0.7%) than the previously reported Yb/Er (20/2 mol%):β-NaYF$_4$ (0.13%). This improved UC performance is probably attributed to the accommodation of high-content Yb sensitizers in the KLu$_2$F$_7$ host. Benefited from the protection of solid oxide glass, the lanthanide-doped K(Lu/Yb)$_2$F$_7$ NCs@glass nanocomposites can experience high-power laser irradiation and produce novel UC performance. Particularly, Er/Tm:K(Lu$_{0.5}$Yb$_{0.5}$)$_2$F$_7$ NCs@glass yields bright white light with a UCQY of 0.2% and is demonstrated to be applicable as a color converter for NIR-laser driven solid-state lighting; Er:K(Yb)$_2$F$_7$ NCs@glass exhibits a remarkable 980 nm laser-induced photothermal effect and is proved to be applicable as a tunable UC emitting tag for high-end anti-counterfeiting. This work exploits a new way to fabricate lanthanide solid-solution fluoride NCs and presents an important advance in exploring innovative high-performance luminescent nano-structured glasses.

Conflicts of interest

The authors declare no competing financial interests.

Acknowledgements

References

1 F. Auzel, *Chem. Rev.*, 2004, **104**, 139–172.
2 X. Zhu, Q. Su, W. Feng and F. Y. Li, *Chem. Soc. Rev.*, 2017, **46**, 1025–1039.
3 H. Dong, L. D. Sun and C. H. Yan, *Chem. Soc. Rev.*, 2015, **44**, 1608–1634.
4 B. Zhou, B. Y. Shi, D. Y. Jin and X. G. Liu, *Nat. Nanotechnol.*, 2015, **10**, 924–936.
5 X. Y. Huang, S. Y. Han, W. Huang and X. G. Liu, *Chem. Soc. Rev.*, 2013, **42**, 173–201.
6 J. T. Xu, P. P. Yang, M. D. Sun, H. T. Bi, B. Liu, D. Yang, S. L. Gai, F. He and J. Lin, *ACS Nano*, 2017, **11**, 4133–4144.
7 D. Hudry, I. A. Howar, R. Popescu, D. Gerthsen and B. S. Richards, *Adv. Mater.*, 2019, **31**, 1900623.
8 D. M. Yang, P. A. Ma, Z. Y. Hou, Z. Y. Cheng, C. X. Li and J. Lin, *Chem. Soc. Rev.*, 2015, **44**, 1416–1448.

This journal is © The Royal Society of Chemistry 2019

J. Mater. Chem. C, 2019, **7**, 14571–14580 | **14579**

9 X. W. Cheng, Y. Pan, Z. Yuan, X. W. Wang, W. H. Su, L. S. Yi, X. J. Xie and L. Huang, *Adv. Funct. Mater.*, 2018, **28**, 1800208.

10 Y. S. Liu, D. T. Tu, H. M. Zhu, R. F. Li, W. Q. Luo and X. Y. Chen, *Adv. Mater.*, 2010, **22**, 3266–3271.

11 J. T. Xu, P. P. Yang, M. D. Sun, H. T. Bi, B. Liu, D. Yang, S. L. Gai, F. He and J. Lin, *ACS Nano*, 2017, **11**, 4133–4144.

12 F. Wang and X. G. Liu, *Chem. Soc. Rev.*, 2009, **38**, 976–989.

13 A. Aebischer, M. Hostettler, J. Hauser, K. Krämer, T. Weber, H. U. Güdel and H. B. Bürgi, *Angew. Chem., Int. Ed.*, 2006, **45**, 2802–2806.

14 K. Krämer, D. Biner, G. Frei, H. U. Güdel, M. P. Hehlen and S. R. Lüthi, *Chem. Mater.*, 2004, **16**, 1244–1251.

15 J. F. Suyver, J. Grimm, K. W. Krämer and H. U. Güdel, *J. Lumin.*, 2005, **114**, 53–59.

16 J. F. Suyver, J. Grimm, M. K. van Veen, D. Binder, K. W. Krämer and H. U. Güdel, *J. Lumin.*, 2006, **117**, 1–12.

17 G. Y. Chen, T. Y. Ohulchanskyy, R. Kumar, H. Agren and P. N. Prasad, *ACS Nano*, 2010, **4**, 3163–3168.

18 J. Wang, R. Deng, M. A. MacDonald, B. L. Chen, J. K. Yuan, F. Wang, D. Chi, T. S. A. Hor, P. Zhang, G. Liu, Y. Han and X. G. Liu, *Nat. Mater.*, 2014, **13**, 157–162.

19 F. Wang, Y. Han, C. Lim, Y. Lu, J. Wang, J. Xu, H. Chen, C. Zhang, M. Hong and X. G. Liu, *Nature*, 2010, **463**, 1061–1065.

20 D. Q. Chen, W. D. Xiang, X. J. Liang, J. S. Zhong, H. Yu, M. Y. Ding, H. W. Lu and Z. G. Ji, *J. Eur. Ceram. Soc.*, 2015, **35**, 859–869.

21 J. B. Zhao, X. L. Zheng, E. P. Schartner, P. Ionescu, R. Zhang, T. L. Nguyen and D. Y. Jin, *Adv. Opt. Mater.*, 2016, **4**, 1507–1517.

22 Q. Pan, Z. Cai, Y. Yang, D. Yang, S. Kang, Z. Chen, J. Qiu, Q. Zhan and G. Dong, *Adv. Opt. Mater.*, 2019, **7**, 1801482.

23 S. F. Zhou, N. Jiang, K. Miura, S. Tanabe, M. Shimizu, M. Sakakura, Y. Shimotsuma, M. Nishi, J. R. Qiu and K. Hirao, *J. Am. Chem. Soc.*, 2010, **132**, 17945–17952.

24 A. Herrmann, M. Tylkowski, C. Bocker and C. Rüssel, *Chem. Mater.*, 2013, **25**, 2878–2884.

25 C. G. Lin, C. Bocker and C. Rüssel, *Nano Lett.*, 2015, **15**, 6764–6769.

26 P. P. Fedorov, A. A. Luginina and A. I. Popov, *J. Fluorine Chem.*, 2015, **172**, 22–50.

27 X. H. Xu, W. F. Zhang, D. Yang, W. Lu, J. B. Qi and S. F. Yu, *Adv. Mater.*, 2016, **28**, 8045–8050.

28 J. S. Zhong, D. Q. Chen, Y. Z. Peng, Y. D. Lu, X. Chen, X. Y. Li and Z. G. Ji, *J. Alloys Compd.*, 2018, **763**, 34–48.

29 X. F. Liu, J. J. Zhou, S. F. Zhou, Y. Z. Yue and J. R. Qiu, *Prog. Mater. Sci.*, 2018, **97**, 38–96.

30 X. Y. Li, D. Q. Chen, F. Huang, G. C. Chang, J. J. Zhao, X. S. Qiao, J. C. Xu, X. H. Du and M. Yin, *Laser Photonics Rev.*, 2018, **12**, 1800030.

31 Q. Cheng, J. Sui and W. Cai, *Nanoscale*, 2012, **4**, 779–784.

32 J. K. Chen, Y. Z. Peng, X. Y. Li, W. Chen, H. Huang, L. Lin and D. Q. Chen, *J. Mater. Chem. C*, 2019, **7**, 4109.

33 D. Q. Chen, Y. Z. Peng, X. Y. Li, J. S. Zhong, H. Huang and J. K. Chen, *ACS Appl. Mater. Interfaces*, 2019, **11**, 30053.

34 A. Pandey, V. K. Rai, V. Kumar, V. Kumar and H. C. Swart, *Sens. Actuators, B*, 2015, **209**, 352–358.